Sensorless Synchronous Reluctance Motor Drives: Auxiliary Flux based Position Observer

Sensorless Synchronous Reluctance Motor Drives: Auxiliary Flux based Position Observer

Anantaram varatharajan, Gianmario Pellegrino, *Senior Member, IEEE,* and Eric Armando, *Senior Member, IEEE,*

***Abstract*—The concept of auxiliary flux vector is defined for the nonlinear magnetic model of a synchronous reluctance (SyR) machine. An auxiliary flux based position observer is developed to circumvent the stability problems of other schemes, notably active flux position observer, without compromising on the simplicity. Stability analysis and sensitivity to parameter errors are presented. The proposed observer is augmented with high-frequency signal injection based position estimation for sustained operation at low speeds region. Proposed technique is experimentally validated on a 1.1 kW SyR machine test bench.**

***Index Terms*—Synchronous reluctance machine, sensorless control, auxiliary flux vector, stability.**

I. Introduction

Control of synchronous machines without a position transducer finds importance in industrial applications and, more recently, in automotive sector for cost reduction and reliability. Many low speed sensorless control techniques rely on high-frequency excitation approach to exploit the differential saliency for position estimation. This comprises of schemes based on: i) continuous excitation using periodic signal injection [1], [2] and ii) discontinuous excitation schemes [3]–[5]. Continuous excitation schemes based on the square-wave voltage injection at half the switching frequency is shown to benefit from simpler demodulation stage and higher bandwidth capabilities in [6]–[8]; this is used in the present work. The high-frequency excitation approach is accompanied with acoustic noise and reduced available voltage for torque production. Hence, at medium to high speed region, it is relegated in the favor of fundamental wave excitation approach for its general better performance [9]–[11].

An active flux based observer is a state of art technique reported in literature [12], [13] where the position error signal is derived from the discrepancy between the observed and the current model along the q-axis. However, it suffers from instability at braking and at high speeds motoring regions as demonstrated in [14], [15]. To circumvent instability, [14] proposed a flux observer with adaptive gain in dq rotor reference frame, to decouple the dynamics of flux and position observers. The additional degree of freedom is exploited to impose a constant damping of the flux observer poles. Alternatively, an adaptive projection vector for position error estimation (APP) scheme was developed in [15] where the instability was addressed by designing an operating point dependent APP vector. Beyond APP, this paper proposes a new observer scheme using a different projection vector, still retaining the simplicity and ease of computation of previous schemes and using the same mathematical foundation of error projection vectors introduced in [14] and further developed in [15] [16].

The concept of auxiliary flux vector is defined and used for designing the new projection vector and thus the new sensorless control system. Being based on the fundamental back-emf or flux linkage waves, the proposed observer is supplemented with a high-frequency excitation scheme for operation in the low speeds region. The paper employs a square wave voltage injection scheme for control under sustained load torque at standstill and very low speed. The transition between the two models is also addressed in the paper.

The notation and symbols are introduced in Section II. The main features of the paper are enumerated as follows:

1) The concept of auxiliary flux vector for a SyR machine is defined in Section II for a nonlinear magnetic model.
2) A position observer based on the auxiliary flux vector is designed in Section III.
3) Stability analysis is presented to analytically evaluate the feasibility of control at all operating regions.
4) The sensitivity to parameter errors in flux map is addressed and the resulting steady-state position error is evaluated.
5) Section IV describes a high-frequency square voltage injection with flux demodulation scheme for position estimation at low speeds region. A linear speed-dependent fusion ensures smooth transition.

Section V presents the experimental validation of the proposed sensorless technique on a 1.1 kW SyR machine test bench and Section VI concludes the paper.

II. Sensorless Control System

The electrical rotor position is θ and the electrical angular speed is $\omega = s\,\theta$ where s is the differential operation $\frac{\mathrm{d}}{\mathrm{d}t}$. Estimated vectors are represented by the superscript $\hat{}$. The orthogonal rotational matrix is $\mathbf{J} = \left[\begin{smallmatrix} 0 & -1 \\ 1 & 0 \end{smallmatrix}\right]$ and $\mathbf{I}$ is the identity matrix.

Real space vectors will be used; for example, the stator current is $\boldsymbol{i}_{\hat{d}\hat{q}} = [i_{\hat{d}}, i_{\hat{q}}]^{\mathrm{T}}$ where $i_{\hat{d}}$ and $i_{\hat{q}}$ are the vector components in estimated rotor reference frame. Space vectors in the stationary reference frame are denoted by subscript $\alpha\beta$.

This work was supported by the Power Electronics Innovation Center (PEIC) of Politecnico di Torino, Italy. *(Corresponding author: Anantaram Varatharajan)*

A. Varatharajan, G. Pellegrino and E. Armando are with the Department of Energy, Politecnico di Torino, Turin 10129, Italy. (email: anantaram.varatharajan@polito.it; gianmario.pellegrino@polito.it; eric.armando@polito.it)

A. Mathematical Model of a SyR Machine

The machine model is expressed in coordinates of estimated rotor reference frame, denoted by subscript $\hat{dq}$, whose d-axis is at $\hat{\theta} = \theta - \tilde{\theta}$, where $\tilde{\theta}$ is the position error. The voltage equation of a SyR machine is given by

$$s\,\boldsymbol{\lambda}_{\hat{dq}} = \boldsymbol{v}_{\hat{dq}} - R_s \boldsymbol{i}_{\hat{dq}} - \hat{\omega}\,\mathbf{J}\,\boldsymbol{\lambda}_{\hat{dq}} \tag{1}$$

where R_s is the stator resistance and $\boldsymbol{\lambda}_{\hat{dq}}$ is the stator flux linkage. The stator flux linkage and its time-derivative are expressed as

$$\boldsymbol{\lambda}_{\hat{dq}} = \mathrm{e}^{\mathbf{J}\tilde{\theta}}\,\boldsymbol{L}\,\mathrm{e}^{-\mathbf{J}\tilde{\theta}}\,\boldsymbol{i}_{\hat{dq}} \tag{2a}$$

$$s\,\boldsymbol{\lambda}_{\hat{dq}} = \mathrm{e}^{\mathbf{J}\tilde{\theta}}\,\boldsymbol{L}_{\partial}\,\mathrm{e}^{-\mathbf{J}\tilde{\theta}}\,s\,\boldsymbol{i}_{\hat{dq}} \tag{2b}$$

where $s\,\tilde{\theta} = 0$ is assumed. The incremental and apparent inductance matrices are denoted by

$$\boldsymbol{L}_{\partial}(\boldsymbol{i}_{dq}) = \begin{bmatrix} l_d & l_{dq} \\ l_{dq} & l_q \end{bmatrix} \quad \boldsymbol{L}(\boldsymbol{i}_{dq}) = \begin{bmatrix} L_d & 0 \\ 0 & L_q \end{bmatrix} \tag{3}$$

where l_d, l_q represents the incremental inductance along direct d and quadrature q axis, respectively, while l_{dq} is the cross-saturation term. Apparent inductances are defined likewise. All quantities are functions of $\boldsymbol{i}_{dq}$. The electromagnetic torque is given by

$$T = \frac{3p}{2}\,\boldsymbol{i}_{\hat{dq}}^{\mathrm{T}}\,\mathbf{J}\,\boldsymbol{\lambda}_{\hat{dq}} \tag{4}$$

where p is the number of pole pairs.

B. Auxiliary Flux Vector Definition

A key assumption is that the flux linkage estimate from back-emf integration, called voltage model flux estimate, equals the actual flux linkage vector. This is true for those angular frequencies that make the resistance voltage and inverter voltage error negligible, or wherever those voltage components are exactly compensated. Therefore, the voltage model flux estimate will have no dedicated notation and will be indicated as the actual flux linkage.

In generic terms, all fundamental excitation schemes rely on the discrepancy between voltage and current model flux linkage for position estimation.

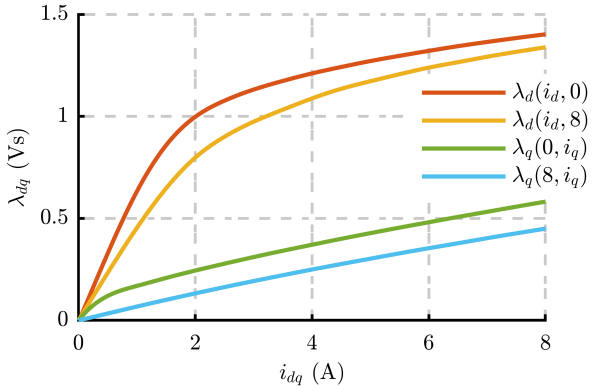

Fig. 1. Flux map of the 1.1 kW SyR motor under test. Experimentally identified with constant speed test reported in [17].

Let $\boldsymbol{\lambda}^i_{\hat{dq}}(\boldsymbol{i}_{\hat{dq}}) = \boldsymbol{L}^i(\boldsymbol{i}_{\hat{dq}}) \cdot \boldsymbol{i}_{\hat{dq}}$ denote the current model flux linkage based on the flux map lookup tables (LUTs), shown in Fig. 1, where $\boldsymbol{L}^i$ is the current model inductance matrix. Then, the discrepancy between the two models can be expressed in the estimated reference frame as

$$\boldsymbol{\lambda}_{\hat{dq}} - \boldsymbol{\lambda}^i_{\hat{dq}} = \mathrm{e}^{\mathbf{J}\tilde{\theta}}\,\boldsymbol{L}(\boldsymbol{i}_{dq}) \cdot \mathrm{e}^{-\mathbf{J}\tilde{\theta}}\,\boldsymbol{i}_{\hat{dq}} - \boldsymbol{L}^i(\boldsymbol{i}_{\hat{dq}}) \cdot \boldsymbol{i}_{\hat{dq}}. \tag{5}$$

Accurate flux map LUTs is assumed, i.e., $\boldsymbol{\lambda}_{dq}(\boldsymbol{i}_{dq}) = \boldsymbol{\lambda}^i_{dq}(\boldsymbol{i}_{dq})$. Then, the stator flux linkage (voltage model) in estimated rotor reference can be represented as

$$\begin{aligned} \boldsymbol{\lambda}_{\hat{dq}}(\boldsymbol{i}_{\hat{dq}}) &= \mathrm{e}^{\mathbf{J}\tilde{\theta}}\,\boldsymbol{\lambda}^i_{dq}(\boldsymbol{i}_{dq}) \\ \implies \boldsymbol{\lambda}_{\hat{dq}}(\boldsymbol{i}_{\hat{dq}}) &= \mathrm{e}^{\mathbf{J}\tilde{\theta}}\,\boldsymbol{\lambda}^i_{dq}(\mathrm{e}^{-\mathbf{J}\tilde{\theta}}\boldsymbol{i}_{\hat{dq}}). \end{aligned} \tag{6}$$

The SyR machine exhibits strong nonlinear magnetic characteristics due to both saturation and cross-saturation phenomenon. Hence, linearizing the term $\boldsymbol{\lambda}^i_{dq}(\mathrm{e}^{-\mathbf{J}\tilde{\theta}}\boldsymbol{i}_{\hat{dq}})$ in (6) around an operating point, marked by a subscript 0, gives

$$\begin{aligned} \boldsymbol{\lambda}^i_{dq}(\mathrm{e}^{-\mathbf{J}\tilde{\theta}}\boldsymbol{i}_{\hat{dq}}) = \boldsymbol{\lambda}^i_{dq}(\boldsymbol{i}_{\hat{dq}0} - \tilde{\theta}\,\mathbf{J}\,\boldsymbol{i}_{\hat{dq}0}) &= \boldsymbol{\lambda}^i_{\hat{dq}0} - \frac{\mathrm{d}\boldsymbol{\lambda}^i_{\hat{dq}}}{\mathrm{d}\boldsymbol{i}_{\hat{dq}}}\,\tilde{\theta}\,\mathbf{J}\,\boldsymbol{i}_{\hat{dq}0} \\ \implies \boldsymbol{\lambda}^i_{dq}(\mathrm{e}^{-\mathbf{J}\tilde{\theta}}\boldsymbol{i}_{\hat{dq}}) &= (\boldsymbol{L}^i - \tilde{\theta}\,\boldsymbol{L}_{\partial}\,\mathbf{J})\,\boldsymbol{i}_{\hat{dq}0}. \end{aligned} \tag{7}$$

In the above derivation, the first order approximation holds for small position error, i.e., a constant incremental inductance in the vicinity of the present operating point. From (2a) and (6), the inductance model accounting position error (IMAP) is derived as

$$\boldsymbol{L} = \boldsymbol{L}^i + \tilde{\theta}\,(\boldsymbol{L}^i - \boldsymbol{L}_{\partial})\,\mathbf{J}. \tag{8}$$

The IMAP was introduced as improved inductance model in [15]. Linearizing (5) gives

$$\boldsymbol{\lambda}_{\hat{dq}}(\boldsymbol{i}_{\hat{dq}}) - \boldsymbol{\lambda}^i_{\hat{dq}}(\boldsymbol{i}_{\hat{dq}}) = \tilde{\theta}\,\boldsymbol{\lambda}^a_{\hat{dq}0} \tag{9}$$

where the auxiliary flux vector $\boldsymbol{\lambda}^a_{\hat{dq}0}$ for nonlinear magnetic model is defined as

$$\boldsymbol{\lambda}^a_{\hat{dq}0} = (\mathbf{J}\,\boldsymbol{L}^i - \boldsymbol{L}_{\partial}\,\mathbf{J})\,\boldsymbol{i}_{\hat{dq}0} = \begin{bmatrix} (l_d - L^i_q)\,i_{\hat{q}0} - l_{dq}\,i_{\hat{d}0} \\ (L^i_d - l_q)\,i_{\hat{d}0} + l_{dq}\,i_{\hat{q}0} \end{bmatrix}. \tag{10}$$

The concept of the auxiliary flux vector was introduced in a projection vector framework in [14].

C. Conventional Inductance Model

In literature, it is common to assume the current model inductance to be equal to the real inductance, i.e.,

$$\boldsymbol{L}(\boldsymbol{i}_{dq}) = \boldsymbol{L}^i(\boldsymbol{i}_{\hat{dq}}). \tag{11}$$

In the following text, (11) will be referred to as inductance model not accounting position error (INAP). Note that INAP is, however, valid only for linear magnetic machines without saturation.

Despite the SyR machine exhibiting nonlinearity, if the INAP is used in (5), the auxiliary flux vector $\hat{\boldsymbol{\lambda}}^{a'}_{\hat{dq}0}$ becomes

$$\boldsymbol{\lambda}^{a'}_{\hat{dq}0} = (\mathbf{J}\,\boldsymbol{L} - \boldsymbol{L}\,\mathbf{J})\,\boldsymbol{i}_{\hat{dq}0} = (L_d - L_q)\begin{bmatrix} i_{\hat{q}0} \\ i_{\hat{d}0} \end{bmatrix}. \tag{12}$$

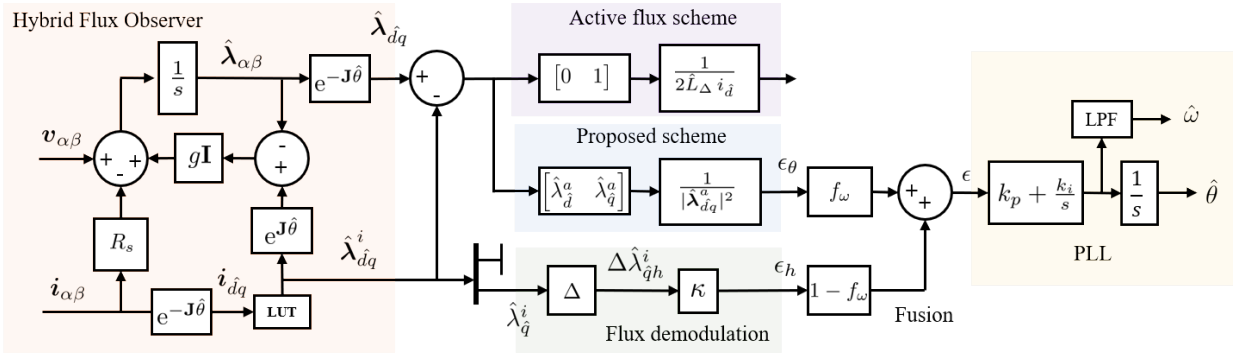

Fig. 2. Hybrid flux observer in stator reference frame with the proposed differential-mode flux based position observer augmented with high-frequency injection for low speeds region. Also shown are the linear speed-dependent fusion mechanism and PLL.

D. Hybrid Flux Observer

The flux observer is defined in the stationary reference frame as

$$s\hat{\boldsymbol{\lambda}}_{\alpha\beta} = \boldsymbol{v}_{\alpha\beta} - R_s \boldsymbol{i}_{\alpha\beta} + \boldsymbol{G}\left(\mathrm{e}^{\mathbf{J}\hat{\theta}}\,\boldsymbol{\lambda}^{i}_{\hat{d}\hat{q}} - \hat{\boldsymbol{\lambda}}_{\alpha\beta}\right) \tag{13}$$

where $\boldsymbol{G} = g\,\mathbf{I}$ is a 2×2 gain matrix. The gain g dictates the dominance of current model on flux observer. The term hybrid indicates that for electrical speeds below g rad/s, the current model flux linkage $\boldsymbol{\lambda}^{i}_{\hat{d}\hat{q}}$ prevails while voltage model flux linkage $\boldsymbol{\lambda}_{\hat{d}\hat{q}}$ for speeds above.

In estimated rotor reference frame, the flux observer in (13) transforms to

$$s\,\hat{\boldsymbol{\lambda}}_{\hat{d}\hat{q}} = \boldsymbol{v}_{\hat{d}\hat{q}} - R_s \boldsymbol{i}_{\hat{d}\hat{q}} - \hat{\omega}\mathbf{J}\,\hat{\boldsymbol{\lambda}}_{\hat{d}\hat{q}} + \boldsymbol{G}\left(\boldsymbol{\lambda}^{i}_{\hat{d}\hat{q}} - \hat{\boldsymbol{\lambda}}_{\hat{d}\hat{q}}\right). \tag{14}$$

To aid in further analysis, the nonlinear flux estimation error dynamics [15] is derived from (1) and (14) as

$$s\,\tilde{\boldsymbol{\lambda}}_{\hat{d}\hat{q}} = -(\boldsymbol{G} + \omega\mathbf{J})\,\tilde{\boldsymbol{\lambda}}_{\hat{d}\hat{q}} + \boldsymbol{G}\,(\boldsymbol{\lambda}_{\hat{d}\hat{q}} - \boldsymbol{\lambda}^{i}_{\hat{d}\hat{q}}) \tag{15}$$

where $\tilde{\boldsymbol{\lambda}}_{\hat{d}\hat{q}} = \boldsymbol{\lambda}_{\hat{d}\hat{q}} - \hat{\boldsymbol{\lambda}}_{\hat{d}\hat{q}}$ is the flux estimation error. Using (10), the flux estimation error dynamics is expressed as a function of position error and auxiliary flux linkage vector as

$$\tilde{\boldsymbol{\lambda}}_{\hat{d}\hat{q}} = (s\mathbf{I} + \boldsymbol{G} + \omega_0\mathbf{J})^{-1}\,\boldsymbol{G}\,\boldsymbol{\lambda}^{a}_{\hat{d}\hat{q}0}\,\tilde{\theta}. \tag{16}$$

III. Fundamental Frequency Excitation - High Speed Model

Let ϵ_θ denote the position error signal of high speed model from the back-emf based fundamental excitation approach. The block diagram of flux and position observer is shown in Fig. 2.

A. Active Flux Position Observer

An active flux based position observer is a state of art sensorless technique that is known for its simplicity and ease of implementation. The active flux is defined under position error as

$$\boldsymbol{\lambda}^{af}_{\hat{d}\hat{q}} = \boldsymbol{\lambda}_{\hat{d}\hat{q}} - L^{i}_{q}\,\boldsymbol{i}_{\hat{d}\hat{q}} = \begin{bmatrix}(L^{i}_{d} - L^{i}_{q})\,i_{\hat{d}}\\ 0\end{bmatrix} + \boldsymbol{\lambda}^{a}_{\hat{d}\hat{q}0}\,\tilde{\theta} \tag{17}$$

where the q-axis component of active flux is proportional to position error. In practice, the position error signal is designed from the observed active flux in HFO as

$$\epsilon_\theta = \frac{1}{2L^{i}_{\Delta}\,i_{\hat{d}}}\begin{bmatrix}0\\1\end{bmatrix}^{\mathrm{T}}(\hat{\boldsymbol{\lambda}}_{\hat{d}\hat{q}} - \boldsymbol{\lambda}^{i}_{\hat{d}\hat{q}}) \tag{18}$$

where $L^{i}_{\Delta} = \frac{L^{i}_{d} - L^{i}_{q}}{2}$. This error function is sensitive to the flux observer gain g and has been shown to suffer from instability at braking and high speed motoring regions in [14], [15].

Note that the active flux position error signal is derived only to provide a quantitative comparison with the proposed auxiliary flux position error signal in terms of simplicity and computational load.

B. Auxiliary Flux Position Observer

It is desired to alleviate the aforementioned instability and yet retain the simplicity of active flux observer. To this end, it can be inferred from (9) that the position error is along the auxiliary flux vector and not along q-axis. Hence, it is intuitive to design an error function of nature

$$\epsilon_\theta = \frac{1}{|\boldsymbol{\lambda}^{a}_{\hat{d}\hat{q}0}|^2}\left(\boldsymbol{\lambda}^{a}_{\hat{d}\hat{q}0}\right)^{\mathrm{T}}(\hat{\boldsymbol{\lambda}}_{\hat{d}\hat{q}} - \boldsymbol{\lambda}^{i}_{\hat{d}\hat{q}}). \tag{19}$$

The proposed error function (19) is similar in structure to (18) while maximizing the amplitude of position error information. It is to be noted that the proposed error function differs from the APP position observer in [15] in that (19) is independent of the operating speed and the flux observer gain $\boldsymbol{G}$.

C. Speed and Position Observer

A conventional phase lock loop (PLL) with a proportional-integral (PI) controller is employed to drive the position error signal ϵ_θ to zero as

$$\hat{\omega} = k_p\,\epsilon_\theta + \int k_i\,\epsilon_\theta\,\mathrm{d}t \qquad \hat{\theta} = \int \hat{\omega}\,\mathrm{d}t \tag{20}$$

where k_p and k_i are the respective gains. The gains of the PLL are tuned for a critically damped response considering $\epsilon = \tilde{\theta}$ by placing the two poles at $s = -\Omega_\omega$:

$$k_p = 2\,\Omega_\omega \qquad k_i = \Omega^2_\omega. \tag{21}$$

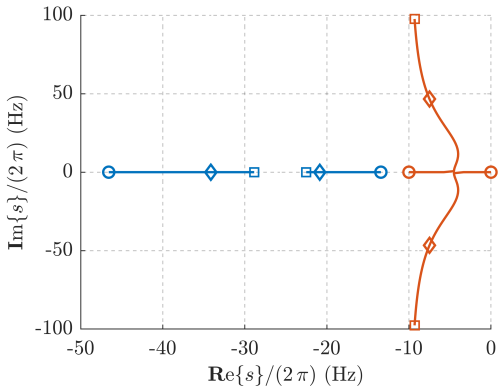

Fig. 3. Locus of poles of position observer for $|\omega|$ = 0.. . . 2 p.u. The circle, diamond and square represents the speeds 0. p.u, 1 p.u and 2 p.u respectively. The poles of PLL are in blue and flux observer in red. Parameters: $g = 2\pi \cdot 10$ rad/s and the gains of PLL are tuned according to (21) with $\Omega_\omega = 2\,\pi \cdot 25$ rad/s.

For the PLL of structure (20), the closed loop transfer function is given by

$$\frac{\hat{\theta}(s)}{\theta(s)} = \frac{(sk_p + k_i)\,K(s)}{s^2 + (sk_p + k_i)\,K(s)} \tag{22}$$

where $K(s) = \epsilon_\theta/\tilde{\theta}$. Note that the position error signal is supplemented with high-frequency model at low speeds as described in section IV.

D. Stability Analysis of Proposed Observer

The stability is studied by analyzing the dynamics of closed loop transfer function of the position observer. Using (9), the linearized form of the error signal (19) becomes

$$\epsilon_\theta = \frac{1}{|\boldsymbol{\lambda}^a_{\hat{d}q0}|^2}\left(\boldsymbol{\lambda}^a_{\hat{d}q0}\right)^{\mathrm{T}}\left(\boldsymbol{\lambda}^a_{\hat{d}q0}\,\tilde{\theta} - \tilde{\boldsymbol{\lambda}}_{\hat{d}q}\right). \tag{23}$$

It follows from the flux estimation error dynamics (16) that the transfer function between the position error signal and position error is

$$K(s) = \frac{\epsilon_\theta}{\tilde{\theta}} = \frac{\left(\boldsymbol{\lambda}^a_{\hat{d}q0}\right)^{\mathrm{T}}}{|\boldsymbol{\lambda}^a_{\hat{d}q0}|^2}\,(s\,\mathbf{I} + \boldsymbol{G} + \omega_0\mathbf{J})^{-1}\,(s\,\mathbf{I} + \omega_0\mathbf{J})\,\boldsymbol{\lambda}^a_{\hat{d}q0} \tag{24}$$

With $\boldsymbol{G} = g\mathbf{I}$ and simplifying,

$$K(s) = \frac{s^2 + s\,g + \omega_0^2}{(s+g)^2 + \omega_0^2}. \tag{25}$$

The transfer function K is observed to be independent of the operating point $\boldsymbol{i}_{\hat{d}q}$ and the direction of rotation.

Using (25) in (22), the locus of poles of the closed loop transfer function is traced in Fig. 3 for electrical speeds from zero to twice rated. The poles are confined to the second quadrant at all operating points and thus, ensuring stability.

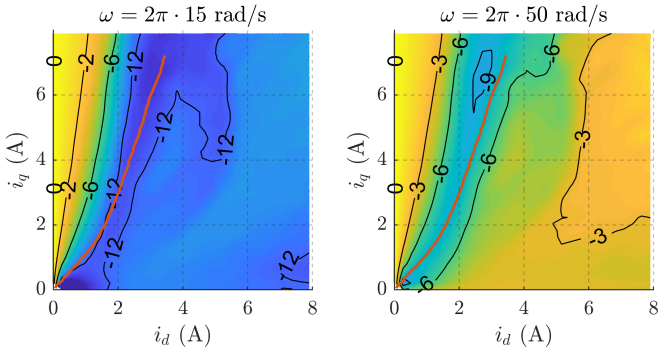

Fig. 4. The steady-state position error $\tilde{\theta}_0$ in degrees (electrical) for +15% error in d-axis flux map, $\hat{\lambda}^i_{\hat{d}} = 0.85\,\lambda_{\hat{d}}$, at different electrical speeds: (a) $\omega = 2\pi \cdot 15$ rad/s; (b) $\omega = 2\pi \cdot 50$ rad/s. In red is the MTPA trajectory.

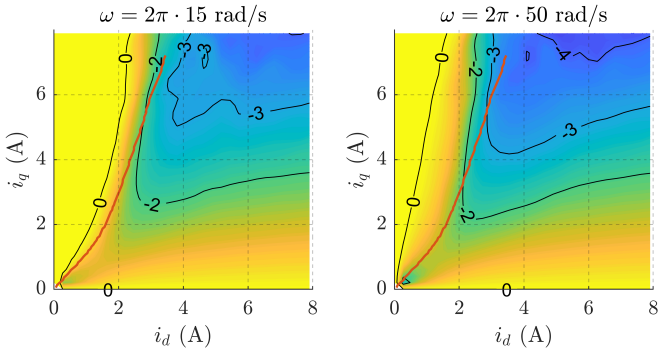

Fig. 5. The steady-state position error $\tilde{\theta}_0$ in degrees (electrical) for +15% error in q-axis flux map, $\hat{\lambda}^i_{\hat{q}} = 0.85\,\lambda_{\hat{q}}$, at different electrical speeds: (a) $\omega = 2\pi \cdot 15$ rad/s; (b) $\omega = 2\pi \cdot 50$ rad/s. In red is the MTPA trajectory.

E. Sensitivity to Parameters Errors

Let the parameter error in the current model flux linkage and the inductance be denoted by $\tilde{\boldsymbol{\lambda}}^i_{\hat{d}q} = \boldsymbol{\lambda}^i_{\hat{d}q} - \hat{\boldsymbol{\lambda}}^i_{\hat{d}q}$ and $\tilde{\boldsymbol{L}} = \boldsymbol{L}^i - \hat{\boldsymbol{L}}^i$, respectively. Then, it follows from (8) and (9) that

$$\boldsymbol{\lambda}_{\hat{d}q}(\boldsymbol{i}_{\hat{d}q}) - \hat{\boldsymbol{\lambda}}^i_{\hat{d}q}(\boldsymbol{i}_{\hat{d}q}) = \tilde{\theta}\,\hat{\boldsymbol{\lambda}}^a_{\hat{d}q0} + \tilde{\boldsymbol{\lambda}}^i_{\hat{d}q} \tag{26}$$

where the auxiliary flux vector is $\hat{\boldsymbol{\lambda}}^a_{\hat{d}q0} = (\mathbf{J}\,\hat{\boldsymbol{L}}^i - \boldsymbol{L}_\partial\,\mathbf{J})\,\boldsymbol{i}_{\hat{d}q0}$. Inculcating the parameter error, the position error function becomes

$$\epsilon_\theta = \frac{\left(\hat{\boldsymbol{\lambda}}^a_{\hat{d}q0}\right)^{\mathrm{T}}}{|\hat{\boldsymbol{\lambda}}^a_{\hat{d}q0}|^2}\,(s\,\mathbf{I} + \boldsymbol{G} + \omega_0\mathbf{J})^{-1}\,(s\,\mathbf{I} + \omega_0\mathbf{J})\,(\hat{\boldsymbol{\lambda}}^a_{\hat{d}q0}\,\tilde{\theta} + \tilde{\boldsymbol{\lambda}}^i_{\hat{d}q}). \tag{27}$$

The steady-state position error can be computed by equating the error signal (27) to zero in steady-state, $\epsilon_\theta\big|_{s=0} = 0$, as

$$\tilde{\theta}_0 = -\frac{\left(\hat{\boldsymbol{\lambda}}^a_{\hat{d}q0}\right)^{\mathrm{T}}}{\omega_0|\hat{\boldsymbol{\lambda}}^a_{\hat{d}q0}|^2}\,(\omega_0\mathbf{I} + g\,\mathbf{J})\,\tilde{\boldsymbol{\lambda}}^i_{\hat{d}q}. \tag{28}$$

Fig. 4(a) and 4(b) shows the contour plots of steady-state position error for +15% error in d-axis, $\hat{\lambda}^i_{\hat{d}} = 0.85\,\lambda_{\hat{d}}$, at the electrical speeds $\omega = 2\pi \cdot 15$ rad/s and $\omega = 2\pi \cdot 50$ rad/s, respectively. It can be discerned that the sensitivity to parameter error is high at lower speeds with position error of

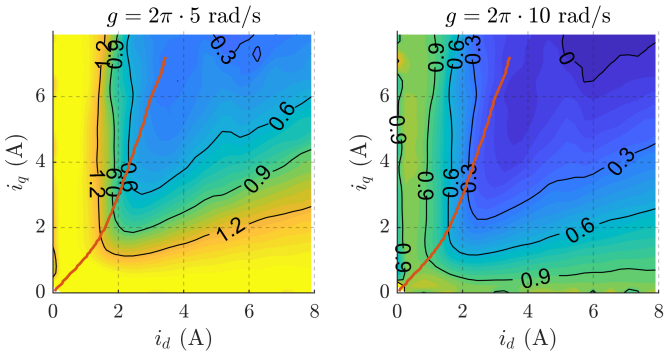

Fig. 6. The steady-state value of K in (31) for error function along auxiliary flux vector based on the INAP at $\omega = 2\pi \cdot 10$ rad/s: (a) $g = 2\pi \cdot 5$ rad/s; (b) $g = 2\pi \cdot 10$ rad/s. In red is the MTPA trajectory.

$\approx -12°$ along the MTPA trajectory. Fig. 5 reports the similar test for +15% error in q-axis, $\hat{\lambda}^i_{\hat{q}} = 0.85\,\lambda_{\hat{q}}$; the maximum position error is $\approx -3°$. It is observed to be less sensitive than d-axis due to the smaller absolute error ($\tilde{L}_q < \tilde{L}_d$).

As the low speed position estimation deteriorates under parameter error and is potentially unstable, it is recommended to switch to the high-frequency excitation schemes for operations at very low speeds.

F. Shortcomings of INAP-based Auxiliary Flux Observer

The position error function in (19) is constructed using the auxiliary flux vector with IMAP (10). If INAP is used instead, the error function defined along the auxiliary flux vector in (12) is

$$\epsilon_\theta = \frac{1}{|\boldsymbol{\lambda}^{a'}_{\hat{d}q0}|^2} \left(\boldsymbol{\lambda}^{a'}_{\hat{d}q0}\right)^{\mathrm{T}} (\hat{\boldsymbol{\lambda}}_{\hat{d}q} - \boldsymbol{\lambda}^{i}_{\hat{d}q}). \tag{29}$$

It can be shown that the error function of the INAP-based auxiliary flux observer is equivalent to the fundamental saliency technique proposed in [18]. The transfer function between the position error signal and position error is expressed in terms of the two auxiliary flux vectors, with IMAP $\boldsymbol{\lambda}^{a}_{\hat{d}q0}$ and with INAP $\boldsymbol{\lambda}^{a'}_{\hat{d}q0}$, as

$$K(s) = \frac{\left(\boldsymbol{\lambda}^{a'}_{\hat{d}q0}\right)^{\mathrm{T}}}{|\boldsymbol{\lambda}^{a'}_{\hat{d}q0}|^2} \left(s\,\mathbf{I} + \boldsymbol{G} + \omega_0 \mathbf{J}\right)^{-1} \left(s\,\mathbf{I} + \omega_0 \mathbf{J}\right) \boldsymbol{\lambda}^{a}_{\hat{d}q0}. \tag{30}$$

The steady-state value of K attests to the amplitude of position error signal, given by

$$K\big|_{s=0} = \frac{\omega_0^2}{g^2 + \omega_0^2} \left[\frac{\left(\boldsymbol{\lambda}^{a'}_{\hat{d}q0}\right)^{\mathrm{T}} \boldsymbol{\lambda}^{a}_{\hat{d}q0}}{|\boldsymbol{\lambda}^{a'}_{\hat{d}q0}|^2} + \frac{g}{\omega_0} \frac{\left(\boldsymbol{\lambda}^{a'}_{\hat{d}q0}\right)^{\mathrm{T}} \mathbf{J} \boldsymbol{\lambda}^{a}_{\hat{d}q0}}{|\boldsymbol{\lambda}^{a'}_{\hat{d}q0}|^2} \right]. \tag{31}$$

It is worth reminding that, unlike (25), the transfer function (31) does depend on the operating point $\boldsymbol{i}_{\hat{d}q}$. In this sense, equation (31) is also a metric of the shortcomings of using INAP-based auxiliary flux vector.

Fig. 6 shows the contour plot of (31) at electrical speed of $\omega = 2\pi \cdot 10$ rad/s in motoring operation for two different values of flux observer gain g. It is discerned that the amplitude of position error signal deteriorates at high load and with increasing g, revealing critical regions for stability. This highlights the susceptibility of INAP and the significance of IMAP.

IV. High Frequency Excitation - Low Speed Model

Let ϵ_h denote the position error signal of the low speed model from high-frequency excitation approach. The components of high-frequency injected signal in estimated rotor reference frame are denoted by subscript $\hat{d}qh$. For a pulsating voltage injection of magnitude v_h and frequency ω_h along $\hat{d}$ axis, the high-frequency flux is given by

$$\boldsymbol{v}_{\hat{d}qh} = v_h \begin{bmatrix} \cos(\omega_h \mathrm{t}) \\ 0 \end{bmatrix} \implies \boldsymbol{\lambda}_{\hat{d}qh} = \frac{v_h}{\omega_h} \begin{bmatrix} \sin(\omega_h \mathrm{t}) \\ 0 \end{bmatrix}. \tag{32}$$

A. Current Demodulation

In the current demodulation scheme, the error signal ϵ_h is proportional to the high-frequency current in q-axis, $i_{\hat{q}h}$. It follows from (2b) that

$$\boldsymbol{i}_{\hat{d}qh} = \mathrm{e}^{\mathbf{J}\tilde{\theta}}\, \boldsymbol{L}_\partial^{-1}\, \mathrm{e}^{-\mathbf{J}\tilde{\theta}}\, \boldsymbol{\lambda}_{\hat{d}qh} \tag{33a}$$

$$\implies i_{\hat{q}h} = \frac{-l_\Delta\, \sin(2\tilde{\theta}) - l_{dq}\, \cos(2\tilde{\theta})}{l_d l_q - l_{dq}^2}\, \frac{v_h\, \sin(\omega_h \mathrm{t})}{\omega_h} \tag{33b}$$

where $l_\Delta = \frac{l_d - l_q}{2}$.

The position error signal is obtained by demodulating (33b) with a heterodyne process. It results in a steady-state position error due to the cross-saturation phenomenon [13], given by

$$\tilde{\theta}_0 = -\frac{1}{2} \tan^{-1} \frac{l_{dq}}{l_\Delta}. \tag{34}$$

B. Flux Demodulation

The demodulation of q-axis high-frequency flux, instead of current, is shown to alleviate the cross-saturation effects [13]. Assuming accurate incremental inductance, the high-frequency current model flux linkage is given by

$$\boldsymbol{\lambda}^{i}_{\hat{d}qh} = \boldsymbol{L}_\partial\, \mathrm{e}^{\mathbf{J}\tilde{\theta}}\, \boldsymbol{L}_\partial^{-1}\, \mathrm{e}^{-\mathbf{J}\tilde{\theta}}\, \boldsymbol{\lambda}_{\hat{d}qh}. \tag{35}$$

Linearizing for small position error,

$$\lambda^{i}_{\hat{q}h} = 2\tilde{\theta}\, \frac{-l_q\, l_\Delta + l_{dq}^2}{l_d l_q - l_{dq}^2}\, \frac{v_h\, \sin(\omega_h \mathrm{t})}{\omega_h}. \tag{36}$$

Through the heterodyne process with a low pass filter (LPF), the error signal is obtained as

$$\epsilon_h = \frac{\omega_h (l_d l_q - l_{dq}^2)}{v_h (-l_q\, l_\Delta + l_{dq}^2)}\, \mathrm{LPF}\left[\lambda^{i}_{\hat{q}h} \cdot \sin(\omega_h \mathrm{t})\right]. \tag{37}$$

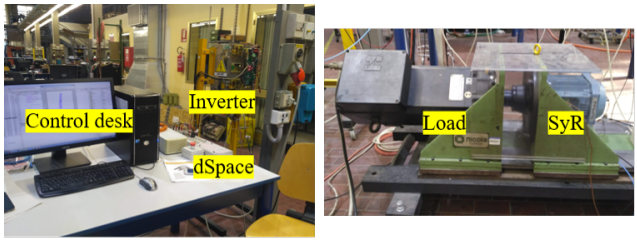

Fig. 7. Experimental Setup of 1.1 kW SyR motor under test on a dspace DS1103 control platform at a sampling frequency of 5 kHz.

TABLE I
MOTOR PARAMETERS

Parameters	Symbol	Values	Units
Rated power	P_n	1.1	kW
Rated voltage	V_n	340	V
Rated speed	ω_n	1500	rpm
Rated current	I_n	2.3	A
Rated torque	T_n	7.1	Nm
Pole pairs	p	2	-
Stator resistance	R_s	6.8	Ω
Shaft inertia	J	0.04	kgm^2

C. Square Wave Voltage Injection

The low pass filter in the demodulation stage (37) hinders the maximum achievable bandwidth of the position observer. This is circumvented with a square wave voltage injection at half the switching frequency [8] as

$$v_{\hat{d}h}^k = v_h \cos(\pi k) = \begin{cases} +v_h, & \text{if } k == 2n \\ -v_h, & \text{if } k == 2n+1 \end{cases} \tag{38}$$

where n is an integer and the superscript k denotes the discrete domain representation of k^{th} sampling instant.

Let Δ symbolize the operation $\Delta x^k = x^k - x^{k-1}$. Then, the error signal in (37) simplifies to

$$\epsilon_h = \kappa\, \Delta\lambda_{\hat{q}h}^i \qquad \kappa = \frac{l_d l_q - l_{dq}^2}{(-l_q\, l_\Delta + l_{dq}^2)\, v_h\, \cos(\pi k)\, T_s} \tag{39}$$

where T_s is the sampling time.

At very high loads, the incremental inductance of the d-axis diminishes due to the magnetic saturation, as is evident from Fig. 1. Consequently, the incremental saliency becomes weak, threatening the stability of the position observer. Thus, the over-load operations are not recommended at low speeds.

D. Fusion Structure

The position observer is designed to transition from low to high speed model at the cross-over frequency g, akin to the flux observer. To refrain from sharp discontinuous transition and chattering, the two position models are fused together with a linear speed-dependent fusion coefficient f_ω as

$$\epsilon = f_\omega \cdot \epsilon_\theta + \big(1 - f_\omega\big) \cdot \epsilon_0. \tag{40}$$

The speed dependency of fusion coefficient is defined as

$$f_\omega = \begin{cases} 0, & \text{if } |\hat{\omega}| < g - \omega_g \\ 1, & \text{if } |\hat{\omega}| > g + \omega_g \\ \frac{g+\omega_g - |\hat{\omega}|}{2\omega_g}, & \text{otherwise} \end{cases} \tag{41}$$

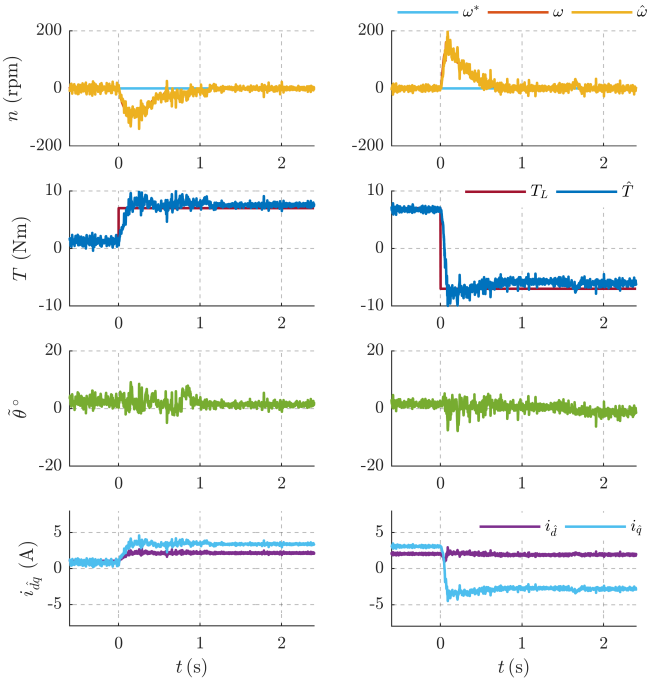

Fig. 8. Test for dynamic stiffness with rated load torque step at standstill: (a) $T_L = 0 \rightarrow 7.1$ Nm at $t = 0$ s; (b) $T_L = +7.1 \rightarrow -7.1$ Nm at $t = 0$ s

where ω_g signifies the span of transition on either sides of cross-over frequency g. Thus, fusion structure is designed for a smooth transition over the speed span $g - \omega_g$ to $g + \omega_g$.

V. EXPERIMENTAL RESULTS

The proposed sensorless scheme is validated experimentally on a 1.1 kW SyR motor on a dspace DS1103 control platform running at a sampling frequency of 5 kHz. A picture of the setup is shown in Fig. 7. The parameters of the SyR motor under test are tabulated in Table I. The SyR machine is sensorless speed controlled while the load torque is imposed by an auxiliary drive.

The PLL gains are tuned for $\Omega_\omega = 2\,\pi \cdot 25$ rad/s. The flux observer gain is $g = 2\,\pi \cdot 10$ rad/s. The span of fusion window is $\omega_g = 2\pi \cdot 2$ rad/s. The speed PI controller is tuned for critical damping at $s = -2\pi \cdot 1$ rad/s. A minimum current $i_d^{min} = 1$ A is imposed for ensuring saturation of ribs at low speeds and minimum fundamental excitation at high speeds.

The motor parameters reside in the flux map LUTs from where the apparent and incremental inductance matrices are retrieved point by point in real-time; as an example:

$$\hat{l}_d(\boldsymbol{i}_{dq}) = \frac{\hat{\boldsymbol{\Lambda}}_d(i_d + \delta i_d, i_q) - \hat{\boldsymbol{\Lambda}}_d(i_d, i_q)}{\delta i_d} \tag{42}$$

where δi_d is a small value (≈ 10 mA). The other inductances are computed in a similar fashion.

A. Dynamic Stiffness

The test for dynamic stiffness of the low speed model is performed at standstill with a rated step in load torque in Fig. 8(a) and a rated reversal in load torque in Fig. 8(b). In

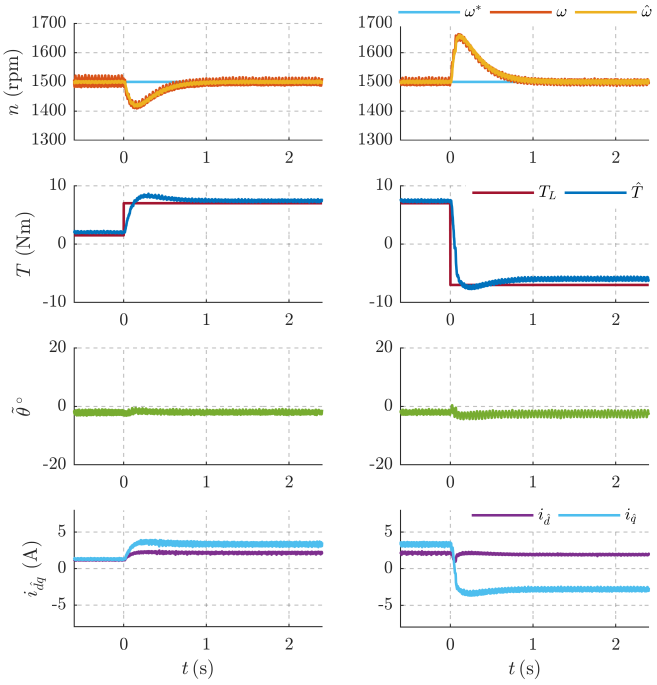

Fig. 9. Test for dynamic stiffness with rated load torque step at rated speed $\omega = 2\pi{\cdot}50$ rad/s: (a) $T_L = 0 \rightarrow 7.1$ Nm at $t = 0$ s; (b) $T_L = +7.1 \rightarrow -7.1$ Nm at $t = 0$ s

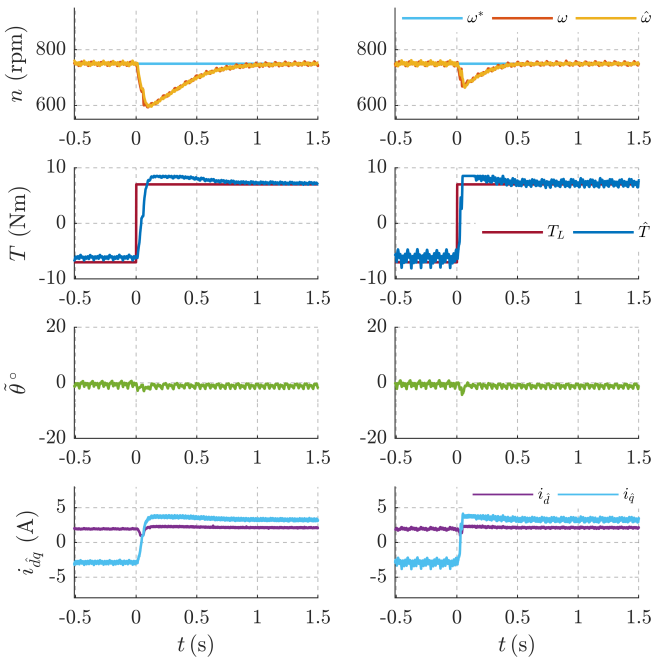

Fig. 10. Comparative torque step test with speed controller tuned for critical damping at: (a) $s = -2\pi \cdot 1$ rad/s; (b) $s = -2\pi{\cdot}3$ rad/s. Rated load torque reversal $T_L = -7.1 \rightarrow +7.1$ Nm at $t = 0$ s and speed $\omega = 2\pi \cdot 25$ rad/s (0.5 p.u).

either case, the position error is observed to be negligible and the speed sag to be around 100 rpm for step torque and 200 rpm for torque reversal test.

Similarly, the test for dynamic stiffness of the high speed model is performed at rated speed in Fig. 9. The position error is observed to be negligible and speed sag to be similar to the former standstill test.

To demonstrate faster dynamic performance, a rated torque reversal is imposed at half-rated speed with the poles of speed PI controller at $s = -2\pi \cdot 1$ rad/s and $s = -2\pi \cdot 3$ rad/s in Fig. 10(a) and 10(b), respectively. A 50% reduction in speed sag is observed from 200 rpm to 100 rpm. As expected, the trade-off is the increase in high-frequency noise that can discerned in the estimated torque.

B. Fusion Evaluation

The competence of fusion is evaluation with a test for dynamic stiffness at the mid-fusion speed, $\omega = g = 2\pi \cdot 10$ rad/s, with rated torque step and rated torque reversal in Fig. 11(a) and 11(b), respectively. Also shown is the fusion coefficient f_ω to illustrate the relative dominance of the two models. The position error is observed to be negligible and the speed sag is similar to former tests at other speeds.

To further demonstrate the smooth transition, an accelerating and decelerating slow speed ramp reference is imposed at half rated torque in Fig. 12(a) and 12(b), respectively. It can be observed that the noise in position error diminished as the control transitions towards the high speed model. No discontinuity is discerned.

C. Transient Performance

The transient performance is evaluated with an accelerating and decelerating speed ramp reference, rate limited at 5000 rpm/s, at no load in Fig. 13(a) and 13(b), respectively. A 50% overload in torque is permitted. It can be observed that the position error during transients is $|\tilde{\theta}_0| < 5^\circ$.

D. Sensitivity to Parameter Errors

The sensitivity to d-axis flux map error is evaluated at rated load torque by imposing an incremental error from +15% ($\hat{\lambda}^i_{\hat{d}} = 0.85\,\lambda_{\hat{d}}$) to -15% ($\hat{\lambda}^i_{\hat{d}} = 1.15\,\lambda_{\hat{d}}$) in steps of 5% increment every 0.5 s at two different speeds. The maximum position error at $\omega = 2\pi \cdot 15$ rad/s in Fig. 14(a) is $\approx 11^\circ$ and at $\omega = 2\pi \cdot 40$ rad/s in Fig. 14(b) is $\approx 7^\circ$. The experimental result corroborates with the estimation of steady-state position error in Fig. 4.

In a similar fashion, the sensitivity to q-axis flux map is evaluated at rated load torque by imposing an incremental error from +15% ($\hat{\lambda}^i_{\hat{q}} = 0.85\,\lambda_{\hat{q}}$) to -15% ($\hat{\lambda}^i_{\hat{q}} = 1.15\,\lambda_{\hat{q}}$) in steps of 5% increment at two different speeds. The maximum position error at either speeds in Fig. 15 is $\approx 3^\circ$. The experimental result corroborates with the estimation of steady-state position error in Fig. 5.

E. Significance of IMAP-based Modeling

To demonstrate the significance of IMAP, a speed ramp reference test at half rated torque under 10% error in d-axis flux map is performed with the error function built with INAP (29) in Fig. 16(a) and with IMAP (19) in Fig. 16(b). Due to the poor amplitude of position error signal (see Fig. 31),

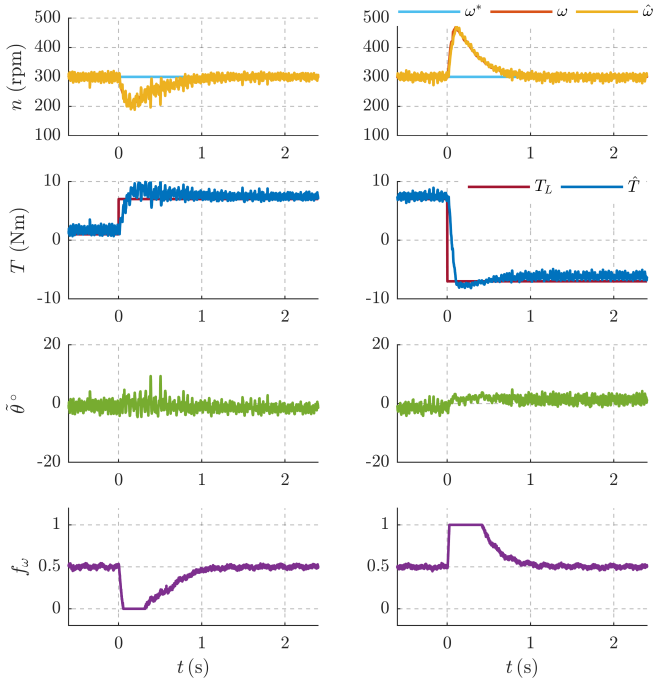

Fig. 11. Load torque step test at mid-fusion speed $\omega = 2\pi \cdot 10$ rad/s (0.2 p.u): (a) $T_L = 0 \rightarrow 7.1$ Nm at $t = 0$ s; (b) $T_L = +7.1 \rightarrow -7.1$ Nm at $t = 0$ s

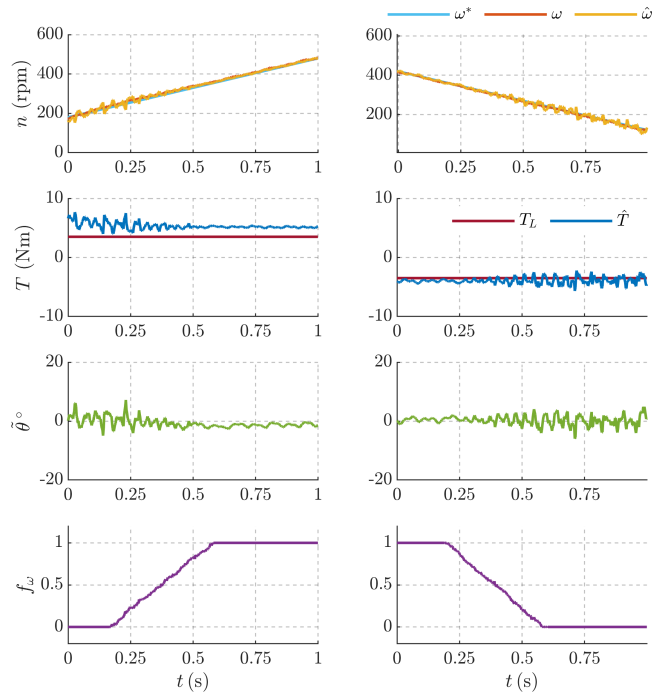

Fig. 12. A slow ramp speed reference to illustrate the smooth fusion between the two models at $T_L = 3.5$ Nm (0.5 p.u).

the sensitivity to parameter error deteriorates to the point of instability as seen in Fig. 16(a). On the other hand, the error function with IMAP is more resilient and does not succumb to instability.

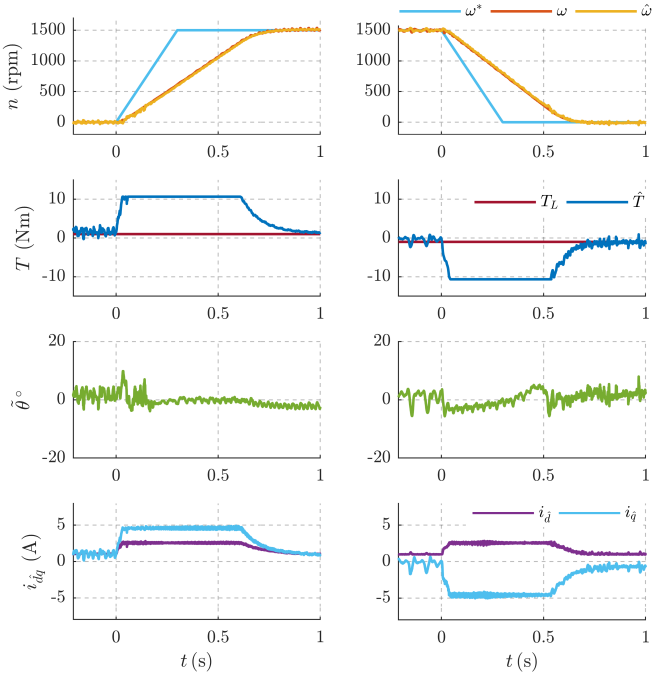

Fig. 13. Transient performance evaluation with speed ramp reference rate limited at 5000 rpm/s: (a) $\omega^* = 0 \rightarrow 1500$ rpm at $t = 0$ s; (b) $\omega^* = 1500 \rightarrow 0$ rpm at $t = 0$ s. A 50% overload in torque is permitted.

VI. Conclusion

The concept of auxiliary flux vector is define and developed for nonlinear magnetic model. An auxiliary flux based position observer is developed in this paper to alleviate the stability problems in active flux position observer while retaining its simplicity and the ease of implementation. Furthermore, this paper illustrates the importance of nonlinear magnetic modeling of IMAP in designing a stable control system. The conventional INAP is shown to be unstable. A stability analysis with combined dynamics of flux and position observer is presented. In addition, the sensitivity of the proposed scheme to parameter error is addressed.

The proposed auxiliary flux position observer is supplemented with square wave voltage injection for low speeds region. A flux demodulation is performed to overcome the cross-saturation error. A speed-dependent linear fusion mechanism is designed for smooth transition between the two models. Finally, the transient and steady-state performance of the proposed sensorless control system is experimentally validated on a 1.1 kW test bench.

References

[1] P. L. Jansen and R. D. Lorenz, "Transducerless position and velocity estimation in induction and salient AC machines," *IEEE Transactions on Industry Applications*, vol. 31, no. 2, pp. 240–247, 1995.

[2] A. Piippo, M. Hinkkanen, and J. Luomi, "Sensorless control of PMSM drives using a combination of voltage model and HF signal injection," in *Conference Record of the 2004 IEEE Industry Applications Conference, 2004. 39th IAS Annual Meeting.*, vol. 2, 2004, pp. 964–970 vol.2.

[3] M. Schroedl and P. Weinmeier, "Sensorless control of reluctance machines at arbitrary operating conditions including standstill," *IEEE Transactions on Power Electronics*, vol. 9, no. 2, pp. 225–231, 1994.

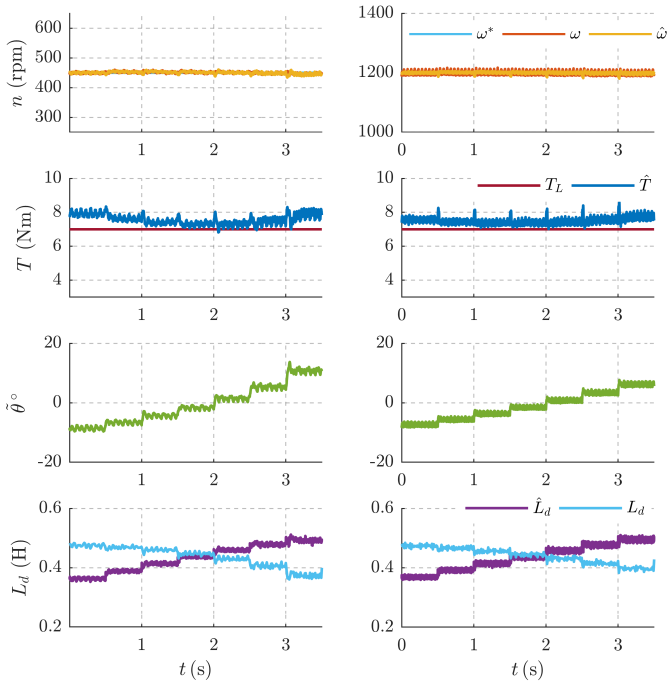

Fig. 14. Sensitivity to error in d-axis flux map, +15% ($\hat{\lambda}^i_{\hat{d}} = 0.85\,\lambda_{\hat{d}}$) → -15% ($\hat{\lambda}^i_{\hat{d}} = 1.15\,\lambda_{\hat{d}}$) in steps of 5% increment every 0.5 s at: (a) $\omega = 2\pi{\cdot}15$ rad/s; (b) $\omega = 2\pi \cdot 40$ rad/s.

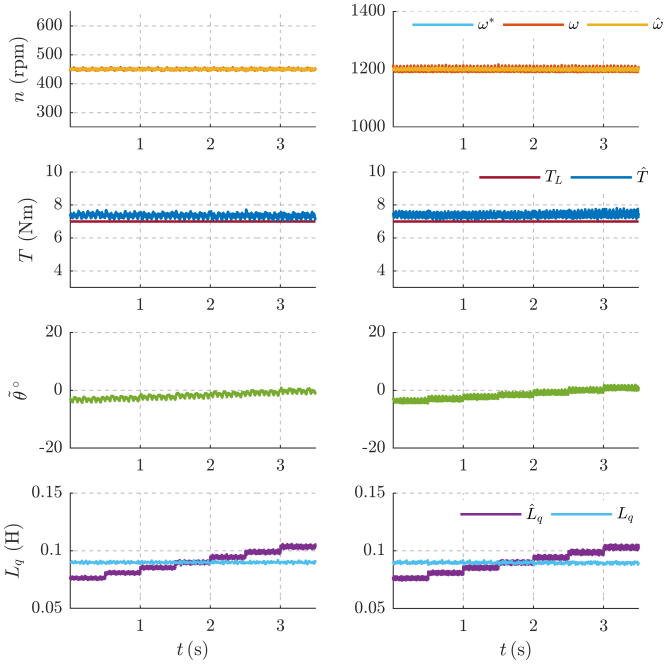

Fig. 15. Sensitivity to error in q-axis flux map, +15% ($\hat{\lambda}^i_{\hat{q}} = 0.85\,\lambda_{\hat{q}}$) → -15% ($\hat{\lambda}^i_{\hat{q}} = 1.15\,\lambda_{\hat{q}}$) in steps of 5% increment every 0.5 s at: (a) $\omega = 2\pi{\cdot}15$ rad/s; (b) $\omega = 2\pi \cdot 40$ rad/s.

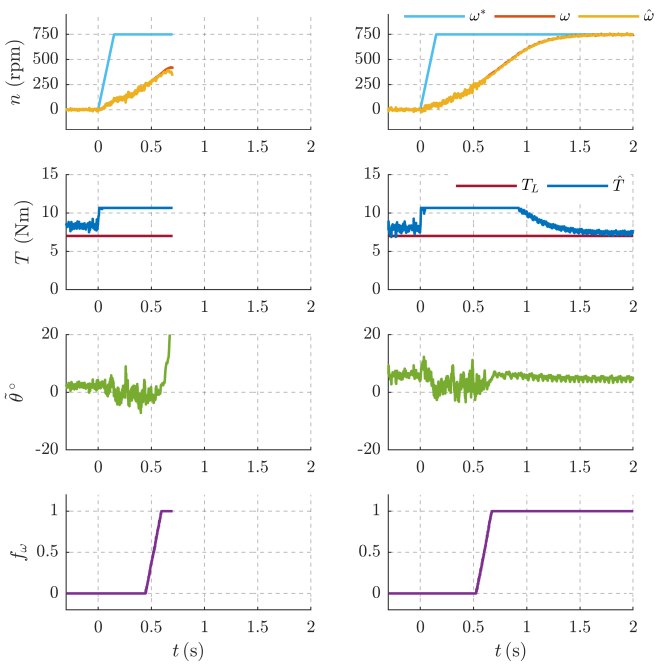

Fig. 16. Operation under +10% error in d-axis: (a) Instability of error function designed with INAP (29); (b) Stability of error function designed with IMAP (19).

[4] R. Morales-Caporal and M. Pacas, "Suppression of saturation effects in a sensorless predictive controlled synchronous reluctance machine based on voltage space phasor injections," *IEEE Transactions on Industrial Electronics*, vol. 58, no. 7, pp. 2809–2817, jul 2011.

[5] A. Varatharajan, P. Pescetto, and G. Pellegrino, "Sensorless synchronous reluctance motor drives: A full-speed scheme using finite-control-set mpc in a projection vector framework," *IEEE Transactions on Industry Applications*, vol. 56, no. 4, pp. 3809–3818, 2020.

[6] Y. D. Yoon, S. K. Sul, S. Morimoto, and K. Ide, "High-bandwidth sensorless algorithm for AC machines based on square-wave-type voltage injection," *IEEE Transactions on Industry Applications*, vol. 47, no. 3, pp. 1361–1370, 2011.

[7] D. Kim, Y. Kwon, S. K. Sul, J. Kim, and R. Yu, "Suppression of Injection Voltage Disturbance for High-Frequency Square-Wave Injection Sensorless Drive With Regulation of Induced High-Frequency Current Ripple," *IEEE Transactions on Industry Applications*, vol. 52, no. 1, pp. 302–312, 2016.

[8] C. E. Hwang, Y. Lee, and S. K. Sul, "Analysis on position estimation error in position-sensorless operation of IPMSM using pulsating square wave signal injection," *IEEE Transactions on Industry Applications*, vol. 55, no. 1, pp. 458–470, 2019.

[9] M. Hinkkanen, T. Tuovinen, L. Harnefors, and J. Luomi, "A Combined Position and Stator-Resistance Observer for Salient PMSM Drives: Design and Stability Analysis," *IEEE Transactions on Power Electronics*, vol. 27, no. 2, pp. 601–609, 2012.

[10] S. C. Agarlita, I. Boldea, and F. Blaabjerg, "High-frequency-injection-assisted 'active-flux'-based sensorless vector control of reluctance synchronous motors, with experiments from zero speed," *IEEE Transactions on Industry Applications*, vol. 48, no. 6, pp. 1931–1939, 2012.

[11] Y. Lee and S. K. Sul, "Model-Based Sensorless Control of an IPMSM With Enhanced Robustness Against Load Disturbances Based on Position and Speed Estimator Using a Speed Error," *IEEE Transactions on Industry Applications*, vol. 54, no. 2, pp. 1448–1459, 2018.

[12] I. Boldea, M. C. Paicu, G. Andreescu, and F. Blaabjerg, ""Active Flux" DTFC-SVM Sensorless Control of IPMSM," *IEEE Transactions on Energy Conversion*, vol. 24, no. 2, pp. 314–322, 2009.

[13] A. Yousefi-Talouki, P. Pescetto, G. Pellegrino, and I. Boldea, "Combined Active Flux and High-Frequency Injection Methods for Sensorless Direct-Flux Vector Control of Synchronous Reluctance Machines," *IEEE Transactions on Power Electronics*, vol. 33, no. 3, pp. 2447–2457, 2018.

[14] M. Hinkkanen, S. E. Saarakkala, H. A. A. Awan, E. Mölsä, and T. Tuovinen, "Observers for Sensorless Synchronous Motor Drives: Framework for Design and Analysis," *IEEE Transactions on Industry Applications*, vol. 54, no. 6, pp. 6090–6100, 2018.

[15] A. Varatharajan and G. Pellegrino, "Sensorless synchronous reluctance motor drives: A general adaptive projection vector approach for position estimation," *IEEE Transactions on Industry Applications*, vol. 56, no. 2, pp. 1495–1504, 2020.

[16] ——, "Sensorless synchronous reluctance motor drives: A projection vector approach for stator resistance immunity and parameter adaptation," *IEEE Transactions on Industry Applications*, pp. 1–10, 2020.

[17] E. Armando, R. I. Bojoi, P. Guglielmi, G. Pellegrino, and M. Pastorelli, "Experimental identification of the magnetic model of synchronous machines," *IEEE Transactions on Industry Applications*, vol. 49, no. 5, pp. 2116–2125, 2013.

[18] P. Landsmann, D. Paulus, P. Stolze, and R. Kennel, "Saliency based encoderless Predictive Torque Control without signal injection for a reluctance synchronous machine," in *Proceedings of 14th International Power Electronics and Motion Control Conference EPE-PEMC 2010*, 2010, pp. S1–10–S1–17.